Journal of Solid State Chemistry 310 (2022) 123006

Contents lists available at ScienceDirect

Journal of Solid State Chemistry

journal homepage: www.elsevier.com/locate/jssc

Effect of doping amount on capacity retention and electrolyte decomposition of $LiNi_{0.5}Mn_{1.5}O_4$-based cathode at high temperature

Tayfun Kocak [a,*], Langyuan Wu [a], Alper Ugur [b], Laifa Shen [a], Francesca De Giorgio [c], Muharrem Kunduraci [d], Xiaogang Zhang [a,*]

[a] Jiangsu Key Laboratory of Electrochemical Energy Storage Technologies, College of Material Science and Engineering, Nanjing University of Aeronautics and Astronautics Nanjing, 210016, PR China
[b] Eskisehir Technical University, Vocational School of Transportation, Eskisehir, 26140, Turkey
[c] National Research Council - Institute of Nanostructured Materials (CNR-ISMN), Via Piero Gobetti, 101, 40129, Bologna, Italy
[d] Tarsus University, Aerospace Engineering Department, Mersin, 33400, Turkey

ARTICLE INFO

Keywords:
High voltage spinel
LNMO
Boron doping
Vanadium doping
Operando differential electrochemical mass spectroscopy (DEMS)

ABSTRACT

The long service life of batteries is one of the most desired parameters for the battery industry and end-users. Several doping elements have been proposed to increase discharge capacity, capacity retention, and rate capability of high voltage $LiNi_{0.5}Mn_{1.5}O_4$ (LNMO) cathode. In this study, two different doping elements, i.e., boron (III) and vanadium (IV), are compared to investigate the doping effect on capacity retention of LNMO-electrodes at high temperatures (50 °C) and extended cycle performance. Different doping amounts are investigated for comparison, i.e., 1, 3, 5, 7, 10 wt% for boron and 10 wt% for vanadium. The actual benefit of doping is observed over extended cycle tests (> 1000 cycles) at 50 °C and 1C. While pristine LNMO electrodes fail after 80 cycles, 10% B-doped LNMO exhibits the highest capacity retention, 80% at 50 °C and 1C after 1200 cycles. The operando differential electrochemical mass spectroscopy results reveal that LNMO electrodes show the highest amount of gas emission (H_2 and O_2) at ~ 4.7 V, where the oxidation of $Ni^{4+/3+}$ and $Ni^{3+/2+}$ occurs. Since high amount doping strategy increases Mn^{3+} amount and, consequently, the charge voltage plateau at ~4 V (Mn^{3+}/Mn^{4+}), this implicitly prevents electrolyte decomposition at high voltage due to decreasing of nickel voltage plateau and less charging step duration at ~ 4.7 V. This investigation shows that the cathode life remarkably can be extended by reducing the nickel content with high amount of doping.

Tayfun Kocak: Conceptualization, Methodology, Investigation, Writing – original draft, Writing – review & editing. Wu Langyuan: Data curation, Writing – review & editing. Alper Ugur: Writing – review & editing. Shen Laifa: Conceptualization, Writing – review & editing. Muharrem Kunduraci: Data curation, Writing – review & editing, Conceptualization. Francesca De Giorgio: Writing – review & editing. Zhang Xiaogang: Conceptualization, Supervision, Project administration.

1. Introduction

Developing long cycle life batteries is critical for zero-emission electric vehicles [1]. The Joint Research Centre of the European Commission expects that up to 900 million electric vehicles (EVs) will be on the road in 2040, and lithium-ion batteries (LIBs) are the most used battery technology in EVs [2]. However, capacity fading during long-term cycling (> 1500 cycles) is still a major challenge for LIBs [3].

Spinel cobalt-free $LiNi_{0.5}Mn_{1.5}O_4$ (LNMO) is considered a promising cathode candidate for next-generation LIBs thanks to its high operating voltage of 4.7 V–4.75 V vs. Li^+/Li, high energy density approaching 650 Wh kg^{-1}, low nickel amount, and fast lithium-diffusion feature [4–6]. Mg-doped LNMO exhibits 87.3% of the initial discharge capacity after 2200 cycles at 10C and 25 °C [5], and Co-doped LNMO retained 94.1% of initial discharge capacity after 1000 cycles at 1C and 25 °C [7]. Therefore, LNMO might be a competitor to replace current cathodes for the battery industry. Also, LNMO spinel cathode is considered by the EU Strategic Research Agenda for Batteries as a promising candidate for the Gen 3b battery generation (forecast market deployment is expected in 2025) for the future vision [8].

The spinel $LiMn_2O_4$ (LMO) structure is the ancestor of the LNMO crystal structure. LMO exhibits structural transition due to Jahn–Teller

* Corresponding authors.
E-mail addresses: tayfun1kocak@gmail.com (T. Kocak), azhangxg@nuaa.edu.cn (X. Zhang).

https://doi.org/10.1016/j.jssc.2022.123006
Received 13 January 2022; Received in revised form 16 February 2022; Accepted 20 February 2022
Available online 3 March 2022

distortion issue [9]. In 1996, Amine et al. proposed the synthesis of Ni element included LMO crystal structure, i.e., LNMO, which could de-/insert Li^+ at ~4.7 V [10]. The most remarkable superiority of LNMO is the higher discharge capacity and cyclability than LMO [6]. However, when cycling is carried out at 55 °C, the LNMO shows severe capacity fading issues [6,11].

During the past two decades, the structural modification of spinel LNMO was extensively investigated to achieve improving capacity retention, particularly at high temperatures (50–60 °C) and maximizing the power density [12,13]. These studies have been mainly focused on, e.g., fine control of particle morphology with temperature or synthesis method, surface coating, and doping research directions [14]. Doping of manganese or nickel in LNMO were actively investigated because doping is one of the most adaptable methods to upscale for commercial production [12]. These doping ions reduced the impurities of $Li_xNi_{1-x}O$ and improved the structural stability of LNMO [15].

The oxidative decomposition of organic solvent-based liquid electrolytes at cathode material interfaces is determined as the major reason for rapid capacity fade in high-voltage LIBs [16]. The electrolyte species decompose at the electrode/electrolyte interface and on the active material surface, increasing the impedance and degrading electrochemical performance [17,18]. Side reactions occur at the LNMO surface and electrolyte interfaces at high charging voltage (~4.7 V) [15]. The formation of a dense 3.1 nm thick fluorine- and phosphorus-rich reaction layer at ~4.75 V on the surface of the LNMO electrode was detected by neutron reflectometry [19]. The gas emission phenomenon is one of the major "symptoms" of electrolyte decomposition at high voltages [20].

Liu et al. tested LNMO half-cells under 20 °C, 40 °C, and 60 °C at 0.5C until 500 cycles and demonstrated that LNMO shows the highest capacity fade at 60 °C (71.5% capacity retention) [21]. High-rate charge/discharge is notably needed when vehicles climb the hills or during fast charging, which increases battery temperature [22]. The durability of batteries at high temperatures is a particularly desirable feature for the battery industry. Therefore, the extended cycle performance at high temperatures is necessary to reveal the actual benefits of the doping strategy on LNMO's capacity retention.

In the present paper, the crystal structures, Mn^{3+} amount, and cycle performance characteristics of pristine and doped-LNMO with two different elements (boron and vanadium) are comprehensively investigated to understand the effect of doping mechanism on electrochemical performance of LNMO-based electrodes at high temperature. Previously, we investigated 10% V-doped LNMO, and it was observed higher capacity retention than pristine and 10% Ti-doped LNMO at 50 °C [23]. Here, different valence shell elements (B^{3+} vs. V^{5+}) are chosen to investigate the effect on capacity retention of LNMO at more than 1000 cycles and 50 °C. Additionally, the effect of doping amount on gas emission (related to electrolyte decomposition and capacity fade) was performed by Operando Differential Electrochemical Mass Spectroscopy (DEMS) measurements.

2. Experimental

2.1. Material preparation

Pristine, commercial LNMO powder (MTI™) was used for the sake of comparative analysis. Pristine LNMO, V-doped LNMO ($LiNi_{0.4}V_{0.1}Mn_{1.5}O_4$), and boron-doped LNMO ($LiNi_{0.5-x}B_xMn_{1.5}O_4$, x = 0.01, 0.03, 0.05, 0.07, and 0.1) samples were prepared and described in our previous work [23]. As-prepared samples were labeled as $LiNi_{0.5}Mn_{1.5}O_4$ (pristine), $LiNi_{0.49}B_{0.01}Mn_{1.5}O_4$ (1 % B-doped), $LiNi_{0.47}B_{0.03}Mn_{1.5}O_4$ (3 % B-doped), $LiNi_{0.45}B_{0.05}Mn_{1.5}O_4$ (5% B-doped), $LiNi_{0.43}B_{0.07}Mn_{1.5}O_4$ (7% B-doped), $LiNi_{0.4}B_{0.1}Mn_{1.5}O_4$ (10% B-doped) and $LiNi_{0.4}V_{0.1}Mn_{1.5}O_4$ (10 % V-doped) respectively. H_3BO_3 (Nanjing Chemical Reagent) was used as boron source and ammonium metavanadate (NH_4VO_3) (SSS Reagent Co., Ltd, Shanghai) as vanadium source. Cathode powders were synthesized at 900 °C for 10 h in a flowing air atmosphere (0.35 Standard Liter Per Minute- SLPM/SIARGO™) with a heating rate of 2 °C min^{-1} and cooling rate of 3 °C min^{-1} to yield the final product.

2.2. Structural, physicochemical, morphological and surface characterization

X-ray diffraction (XRD, Malvern Panalytical Empyrean) incorporating Cu Kα (1.54) radiation was used to characterize the phase structures of all samples. The relative Mn^{3+} content and valence states of the surface components of all samples were determined by X-ray photoelectron spectroscopy (XPS) analysis (PHI5600, Physical Electronics). The XPS spectra were analyzed by using XPSPEAK 4.1 software. The background was corrected using the Shirley method. Raman analysis was carried out between 100 and 800 cm^{-1} by using Horiba Labram Raman exciting at 514.5 nm, using an Argon ion laser. Spectral resolution and power were 2.0 cm^{-1} and 1.0 mW, respectively. The wt.% ratio of B, V, Mn, and Ni elements in the LNMO samples was measured by means of inductively coupled plasma optical emission spectrometry (ICP-OES, Shimadzu-ICPE 9000). The morphological characterization of the samples was carried out with a field emission scanning electron microscope (FESEM-JEOL JSM-6308LV) with an acceleration voltage of 5.0 kV.

Thermogravimetric analyses (TGA) of commercial, synthesized pristine LNMO, 10 % V-doped, and 10% B-doped LNMO were carried out under nitrogen (N_2) and air atmosphere at 5 °C min^{-1} heating rate by Netzsch TG 209F3 Thermogravimetric Analyzer.

2.3. Electrochemical characterization

The positive electrode was prepared by first mixing a slurry containing 80 wt% LNMO-based active material, 10 wt% acetylene black (MTI™), and 10 wt% polyvinylidene fluoride (PVdF) binder (MTI™) and the proper amount of N-methyl-2-pyrrolidone (NMP) as dispersant. The slurries were prepared with planetary ball milling Fritsch Pulverisette™ (200 rpm), coated on aluminum foil, then dried at 60 °C in a vacuum furnace to remove the NMP solvent. The mass loading of the active materials was approximately 5–6 mg cm^{-2}. The electrodes were punched into round disks with diameters of 12 mm, then dried at 60 °C for 18 h in a vacuum oven. The cells were assembled in an argon-filled glovebox (< 0.1 ppm O_2, < 0.1 ppm H_2O) by using 1 M $LiPF_6$ lithium salt dissolved in ethylene carbonate and dimethyl carbonate solution (EC: DMC = 1:1 v/v) as electrolyte (DoDoChem). CR2032 coin cells were assembled with LNMO cathode (12 mm diameter), lithium metal sheet (1 mm thickness and 15 mm diameter) as anode, and borosilicate glass fiber (Whatman™) as separator (16 mm diameter). All coin cell hardware pieces were washed and cleaned with methanol and dried before coin cell assembly.

The electrochemical measurements on each cell were carried out in two electrode-mode at least three times in order to guarantee the reproducibility of the electrochemical data. Before the electrochemical tests, the cells were kept in open-circuit voltage (OCV) for 10 h, then the charge-discharge cycles between 3.5 and 4.9 V were carried out with Neware BTS-5 battery test system at 26 °C and 50 °C. The rate capability test was conducted according to a constant current (CC) charge at 0.1C, 0.2C, 0.5C, 1C, 2C, and 5C up to 4.9 V, then a CC discharge at the corresponding charging rates was carried out. The cycling performance tests were performed at 1C (1C = 147 mA g^{-1}). 5 min-additional constant voltage (CV) charging step was added to 10 B-doped LNMO electrodes at 4.7 V to observe electrolyte degradation and gas emissions at 1C and 50 °C for comparison with and without additional CV step.

CHI760e electrochemical workstation (Chenhua, Shanghai) was used to carry out the cyclic voltammetries (CVs) and electrochemical impedance spectroscopy (EIS) measurements. The CVs were performed on fresh cells by using pristine, B-doped, and V-doped LNMO electrodes as the positive electrode and lithium foil as the negative one, in the voltage range from 3.5 V to 5.0 V at the scanning rate of 0.1 mV s^{-1} at 25 °C. The cycling voltammograms were normalized to the mass of electrode active

material.

The electrochemical impedance spectroscopy (EIS) measurements were carried out by applying a signal with an amplitude of 5 mV in the frequency range of 100 kHz to 0.01 Hz. The EIS measurements of B-doped and V-doped LNMO electrodes were performed in OCV on fresh cells in the 2-electrode mode in the discharge state. The fitting simulation of EIS spectra was carried out by CHI760e equipment software.

Operando Differential Electrochemical Mass Spectroscopy (DEMS) analyses were performed with the Linglu Tech QAS 100 (Pfeiffer Vacuum inside) instrument. Preparation and assembly of half-cell steps of the DEMS cell attachment were carried out in the glovebox. The same half-cell preparation procedure was carried out for DEMS cell attachment with cathode electrode, glass-fiber separator, 40 μL electrolyte, 1 mm thickness lithium metal anode, 1 mm thick metal sheet, and stainless-steel ring. Stainless steel metal tubing with nominal diameters of 1/4 in. and 1/16 in. tube fittings and quick connects were used for DEMS attachment. Then, polypropylene (PP) pipelines were used between DEMS attachment, DEMS equipment, and argon gas tanks. Argon gas served as an inert carrier gas, and its flow rate was set to DEMS attachment 2% (0.24 mL/min) during the electrochemical tests. At the same time, the cells were tested according to galvanostatic charge/discharge cycles (Land battery test system Wuhan, China) at 1C between 3.5 and 4.9 V at 50 °C. The synchronization of the ion current signal with the electrochemical measurements was performed with the help of the computer clock. MTI^{TM} benchtop laboratory furnace was used for heating the DEMS half-cell attachment during the cycling test. Intensities of the ion currents of three selected mass-to-charge ratios were monitored continuously over several hours until the ion currents reached stable background levels. The three monitored ratios were m/z = 2, 32, 44, related to the components H_2, O_2, CO_2, respectively. The dry ice-cooled cold trap was used to entrap volatile electrolyte components to protect the mass spectrometer and enhance its sensitivity.

3. Results and discussions

3.1. Structural, physicochemical, morphological and surface characterization

The synthesis of the disordered *Fd3m* phase was carried out at 900 °C and airflow atmosphere. XRD results of Fig. 1a confirm the formation of disordered *Fd3m* structure in LNMO-based powders, as also proved by our previous studies [23,24]. In Fig. 1b, the pristine LNMO crystal structure has a small amount of NiO peaks at 37.5°, 44° and 63° in the 2 range [1,4]. Liang et al. observed in Mg-doped LNMO both $Li_xNi_{2-x}O_2$ and $Li_xMn_2O_4$ phases (ICSD#50415) with weight fractions of 3.4% and 2.2%, respectively, albeit such impurities could be ignored due to their relatively minor content [5]. Kunduraci et al. studied the effect of synthesis temperature (620–880 °C), Ni element ratio (x = 0.36 to 0.50 $LiNi_xMn_{1.5-x}O_4$), and synthesis atmosphere environment (oxygen and nitrogen gases) on LNMO crystal phases carefully [28]. Their results demonstrated that when the Ni ratio increases, the temperature of disordered *Fd3m* phase formation increases, and the *Fd3m* phase starts at 680 °C in the air atmosphere (21% oxygen) for $LiNi_{0.4}Mn_{1.6}O_4$. Likewise, the ordered structure could be transformed into a disordered structure above 700 °C with the formation of oxygen vacancies and Mn^{3+} ions in the lattice [25]. Cooling speed also affects Mn^{3+} amount and phase fraction (*Fd3m vs. P4$_3$32*). The fast cooling increases disordered phase fraction, as observed where 97.7 wt % (5 °C/min cooling rate) and 78.6 wt % (1 °C/min cooling rate) *Fd3m* phase fractions are formed when applied different cooling rates in the air [25]. In the present study, a 3 °C/min cooling rate was carried out in ambient air.

When the amount of boron doping increases, boron-related impurity appears at 2Θ = 17.4° and 35° (Fig. 1b–c), i.e., $Mn_{2.5}Ni_{0.5}(BO_3)$, as also observed in Ref. [15]. On the other hand, 10 % V-doped LNMO shows impurity-related peaks at 2Θ = 30.83°, 54.7°, and 64.04°, attributed to nickel divanadate $Ni_2(V_2O_6)$ (Fig. 1b) [23].

Ohzuku et al. demonstrated that any occupancy of substituent ions in

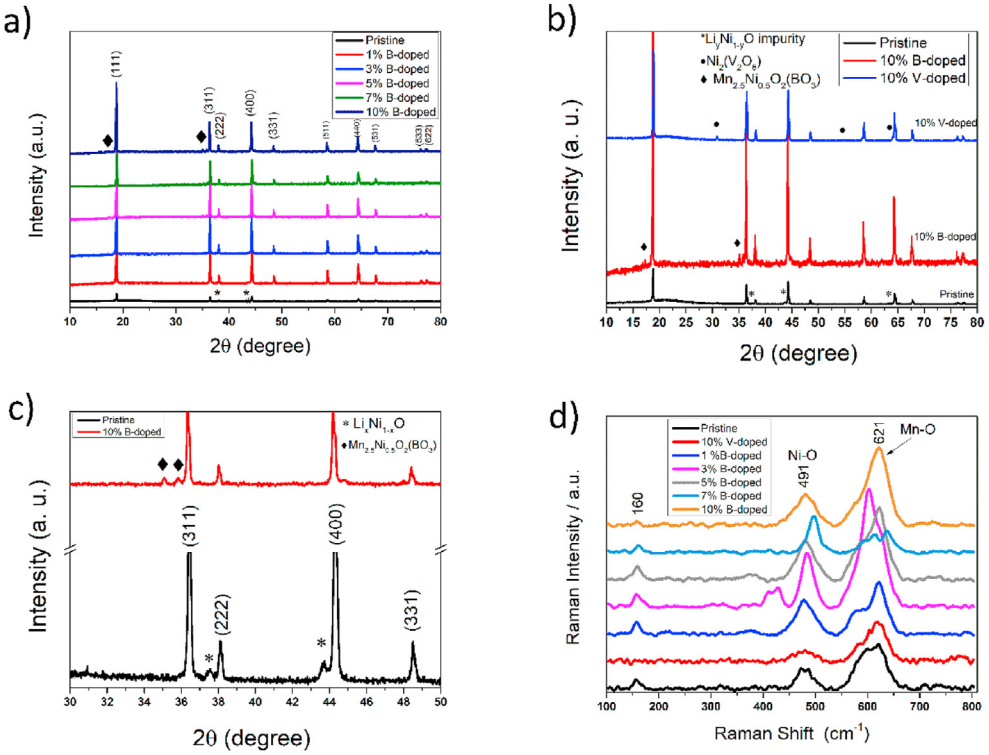

Fig. 1. XRD patterns of LNMO-based powders: (a) pristine, 1% B-doped, 3% B-doped, 5% B-doped, 7% B-doped, and 10% B-doped; (b) pristine, 10% V-doped and 10% B-doped; (c) pristine and 10% B-doped. (The ticks indicate the $Li_xNi_{1-x}O$, $Ni_2(V_2O_6)$, and $Mn_{2.5}Ni_{0.5}(BO_3)$ impurity phases.); (d) Raman spectra of pristine, 1% B-doped, 3% B-doped, 5% B-doped, 7% B-doped, 10% B-doped, and 10% V-doped.

the 8a tetrahedral lithium sites would lead to unfavorable electrochemical performances [26]. The calculated intensity ratios of the (400)/(311) peaks indicate the extent of occupancy of the substituent (Fe-doping) ions in the 8a lithium sites. When Fe ions at the 8a sites increase, the intensity ratios of the (400)/(311) peaks decrease. Similarly, when the B doping amount increases, the (400)/(311) peaks ratio decreases (Table 1).

The ordered *P4$_3$32* and disordered *Fd3m* structures may coexist in all the samples [15,27]. Indeed, Raman spectroscopy analysis was carried out to identify the doping effect of boron and vanadium elements on LNMO ordered (*P4$_3$32*) and disordered (*Fd3m*) phases as supportive analysis to confirm the XRD analysis [27,28].

Fig. 1d shows the Raman spectra of pristine, 10% V-doped, 1% B-doped, 3% B-doped, 5% B-doped, 7% B-doped, and 10% B-doped LNMO powders. The main band differences are observed at around 160 cm^{-1}. The band at 160–166 cm^{-1} for the pristine LNMO is attributed to the ordered *P4$_3$32* structure [27,29,30], and the pristine sample exhibits a stronger band than those of 10% V-doped and 10% B-doped samples.

Additionally, in comparison of boron-doped LNMO samples, the intensity of the band at 160–166 cm^{-1} decreases when wt.% of boron quantity increases. Similarly, 10% B-doped and 10% V-doped samples exhibit the lowest band intensity around 160 cm^{-1}. Zhong et al. observed a similar decreasing band tendency at around 160–166 cm^{-1} for 10% Fe, 10% Cr, and 10% Co-doped to LNMO samples [30]. The splitting of the $F_{2g}^{(3)}$ band at 590 cm^{-1} was often considered as obvious evidence of the ordered structure (*P*4$_3$32) in the spinel [11,25,28,31]. Characteristic peak splitting related to space group *P*4$_3$32 was not detected at ~590 cm^{-1}, suggesting that all the samples have a majority of *Fd3m* structure. Therefore, the Raman spectra analysis proved that vanadium and boron doping lead to the formation of disordered (*Fd3m*) structures for LNMO spinel. The disordered (*Fd3m*) phase is the desired phase since it displays about fifteen-time higher electronic conductivity than the ordered phase at room temperature in the lithiated state [32,33].

B, V, Mn, and Ni wt% ratios in the as-prepared LNMO samples were measured by ICP-OES analysis and reported in Table S1. Fig. 2a shows that the boron wt.% increasing linear trend is observed from 1% B-doped (219 ppm), 3% B-doped (718 ppm), 5% B-doped (1388 ppm), 7% B-doped (3373 ppm), to 10% B-doped (3869 ppm) LNMO, as expected. Fig. 2b shows Mn wt% ratio in the prepared samples. While the Mn mole ratio was constant for each sample preparation, the Mn wt% ratio linearly increased. Fig. 2c shows the Ni wt.% in the as-prepared samples; the Ni wt.% amount linearly decreases except for 7 wt% B-doped LNMO.

The TGA analysis under N_2 and air atmosphere were performed to reveal the thermal stability of LNMO-based powders, i.e., commercial LNMO, laboratory synthesized pristine, 10 % V-doped, and 10% B-doped LNMO powders. Fig. S1 shows the dM/dT vs. T profiles of commercial pristine (747 °C), pristine synthesized (745 °C), 10% V-doped (774 °C), and 10% B-doped LNMO (797 °C) powders under N_2 atmosphere. V-doped and B-doped LNMO samples show the highest exothermic reaction temperatures, probably due to strong bond structure and higher bond dissociation energy. B-doped LNMO (B–O bond energy 809 kJ mol^{-1}) exhibits higher exothermic reaction temperature than V-doped (V–O bond energy 637 kJ mol^{-1}) due to higher bond dissociation energy than Ni–O (366 kJ mol^{-1}) [23].

As widely known, morphologies of active particles, surface orientation, and particle size play a critical role in the long-term cycling stability and rate capability [25,34]. Fig. 3a–d shows the SEM images of pristine and boron-doped (1%, 5%, and 10%) LNMO powders. While pristine (Figs. 3a) and 1% B-doped (Fig. 3b) LNMO display the typical well-defined truncated octahedral crystal structures and smooth surface, 5% B-doped (Figs. 3c) and 10% B-doped (Fig. 3d) LNMO samples exhibit a rough surface. The sharp truncated octahedral edges are observed for 10% V-doped particles at 1000x and 10.000x magnification (Figs. S2a and S2b). Chen et al. synthesized both octahedral and truncated octahedral LNMO particles, demonstrating that truncated octahedral-shaped particles (6 times higher lithium diffusion coefficient) exhibit superior cycling performance than octahedral shape particles, especially at high temperature (55 °C) [28].

Survey XPS spectra of 10 % B-doped LNMO and the peak of B 1s are shown in Fig. S3, and the Mn 2p$_{3/2}$ and Mn 2p$_{1/2}$ of 1%, 3%, 5%, 7%, and 10% B-doped, and 10% V-doped LNMO powders are shown in Figs. S4a–f. The XPS spectrum of B 1s was detected at 191.8 eV for 10% B-doped LNMO, as also observed in Ref. [15]. Fig. 4a shows that for 10% B-doped, the signal of Mn 2p is split into two parts due to the spin-orbit coupling: the Mn2p$_{3/2}$ peak and Mn 2p$_{1/2}$ at approximately 642.8 eV and 653.9 eV, respectively [35,36]. The peak of Mn 2p$_{3/2}$ is divided into two peaks at approximately 641.67 eV and 643.3 eV related to Mn^{3+} and Mn^{4+}, respectively [15]. Fig. 4b shows the peak area ratio of Mn^{+3}/Mn^{+4} of B-doped samples. When wt.% B-doping increases, the Mn^{+3}/Mn^{+4} ratio exhibits an increasing trend. Such an increasing content of Mn^{3+} suggests that the doping process induces part of Mn^{4+} ions to be reduced to Mn^{3+} ions due to charge neutrality [23]. The Mn^{3+}/Mn^{4+} ratios are 0.41, 0.67, 0.62, 1.28, 1.04 and 0.84 for pristine, 1 % B-doped, 3 % B-doped, 5 % B-doped, 7 % B-doped and 10 % B-doped LNMO, respectively (Fig. S3). The results show that Mn^{3+}/Mn^{4+} ratios do not fit ideal linearity due to a lack of control parameters of synthesis [37].

3.2. Electrochemical characterization

Fig. 5a and b shows the cyclic voltammograms of pristine, V-doped, and B-doped LNMO electrodes at 0.1 mV s^{-1} and 25 °C. Two major peaks are visible for all the samples at around 4.75 V, related to the redox couples of Ni^{2+}/Ni^{3+} and Ni^{3+}/Ni^{4+}, and the peak at ~4.0 V is attributed to the Mn^{4+}/Mn^{3+} redox reaction. These results confirm that all the prepared samples exhibit disordered *Fd3m* structure featuring Mn^{3+} content [1].

The difference between the voltages of the second anodic peaks (E_{pa}) related to Ni^{3+}/Ni^{4+} oxidation process and cathodic peaks (E_{pc}), i.e., $\Delta E_p = E_{pa} - E_{pc}$, of pristine, 1% B-doped, 10% B-doped, and 10% V-doped LNMO electrodes are reported in Table S2. When the doping amount increases, the polarization is reduced. The redox peaks of LNMO doped samples are much sharper, and the ΔE_p are more visible at 4.60 V and 4.72 V than for pristine LNMO, which exhibits a much faster charge transport and better kinetic properties. Doping elements reduce the charge balance of Ni^{+4} to Ni^{+3} due to enhanced chemical neutrality, and the two nickel element redox reactions clearly show higher peak splitting [23]. The 10% B-doped and 10% V-doped samples significantly impact the redox process at ~4 V due to the higher Mn^{3+} amount.

The cycling test of doped LNMO electrodes aims at understanding if doping amount and different valence shell elements (B^{3+} vs. V^{5+}) affect the capacity retention and rate capability of LNMO-based electrodes at high temperature. The specific capacity during the rate capability test of pristine, 1%, 3%, 5%, 7%, 10% B-doped and 10% V-doped LNMO electrodes at 50 °C and different C-rates are 0 mAh g^{-1}, 35 mAh g^{-1}, 88 mAh g^{-1}, 101 mAh g^{-1}, 88 mAh g^{-1}, 78 mAh g^{-1}, 97 mAh g^{-1} at 2C, respectively (Fig. 6a). High amount doped cells have higher discharge capacity at high C-rates due to Mn^{3+} amount. A high amount boron or vanadium doping strategy increases Mn^{3+} due to charge neutrality of Mn

Table 1
Comparison of peak intensities of (400) and (311) peaks of pristine, 1% B-doped, 3% B-doped, 5% B-doped, 7% B-doped, 10% B-doped LNMO and 10% V-doped LNMO powders.

Sample Code	(400) peak intensity	(311) peak intensity	(4 0 0)/(311) peaks intensity ratio
Pristine	841	736	1.142
1% B	9088	8962	1.014
3% B	9008	8571	1.050
5% B	8907	8868	1.004
7% B	5512	5362	1.027
10% B	6875	6925	0.992
10% V	1872	1820	1.028

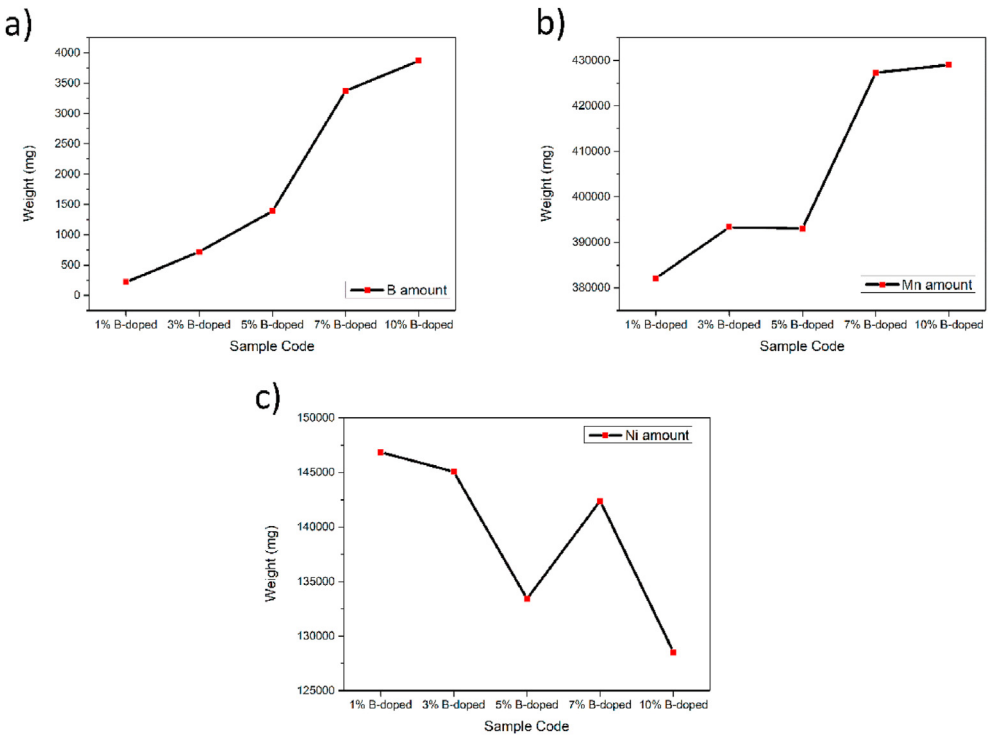

Fig. 2. Comparison of ICP results: (a) B amount, (b) Mn amount and (c) in Ni amount in 1% B-doped, 3% B-doped, 5% B-doped, 7% B-doped, and 10% B-doped LNMO samples.

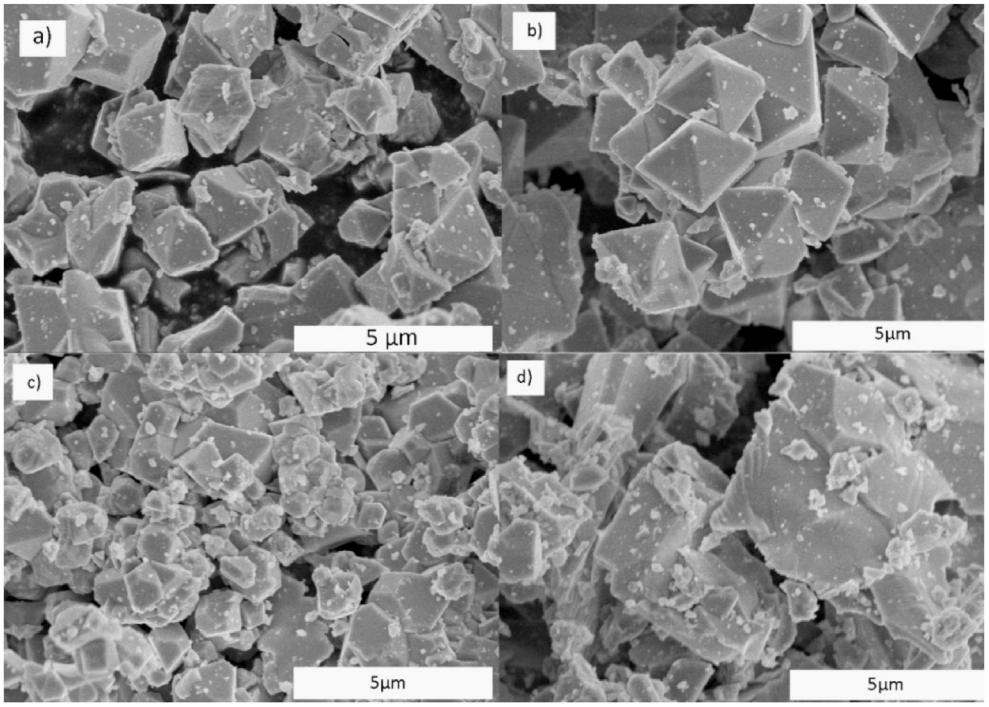

Fig. 3. SEM images of (a) pristine, (b) 1% B-doped, (c) 5% B-doped, and (d) 10% B-doped LNMO powders at 10000x magnification.

element from Mn^{4+} to Mn^{3+} (proved by XPS results at Fig. 4b) [23]. Mn^{3+} increases electronic conductivity and decreases the charge-transfer resistance of LNMO [38]. Differences between low amount doping and high amount doping can be observed clearly at high C-rates (> 2C). Similarly, Cr-doped LNMO and Ru-doped LNMO electrodes exhibited higher discharge capacity than the pristine one at high C-rates [39,40].

When the doping level increases, the first discharge capacity decay occurs due to a decrease of electrochemically active Ni redox couples [11]. The rapid capacity fade and poor rate capability performance of pristine LNMO may be attributed to the long duration of the electrochemical process at ~4.7 V, 0.1C, and 50 °C, where the electrolyte decomposition is facilitated [21,41]. Microcracks may occur on the LNMO surface over extended cycling, thus further accelerating the surface corrosion due to the development of cathode electrolyte interphase

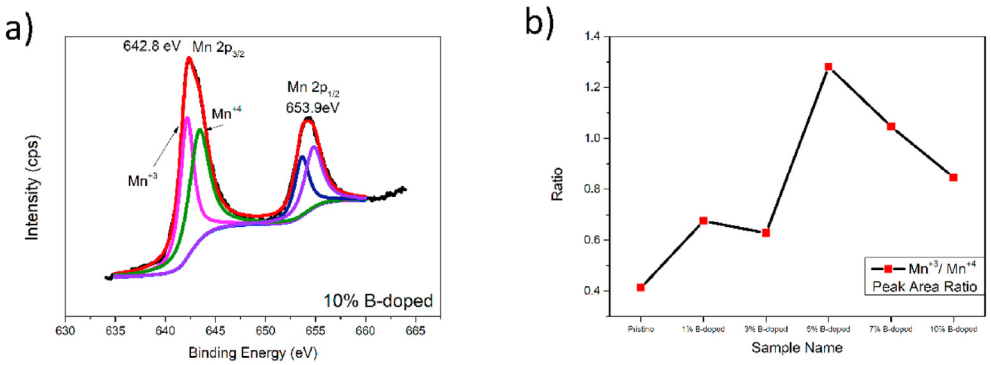

Fig. 4. XPS results of LNMO-based powders: a) XPS spectra Mn $2p_{3/2}$ and Mn $2p_{1/2}$ for 10% B-doped; b) Mn^{3+}/Mn^{4+} peak area ratio of pristine LNMO, 1% B-doped, 3% B-doped, 5% B-doped, 7% B-doped, and 10% B-doped.

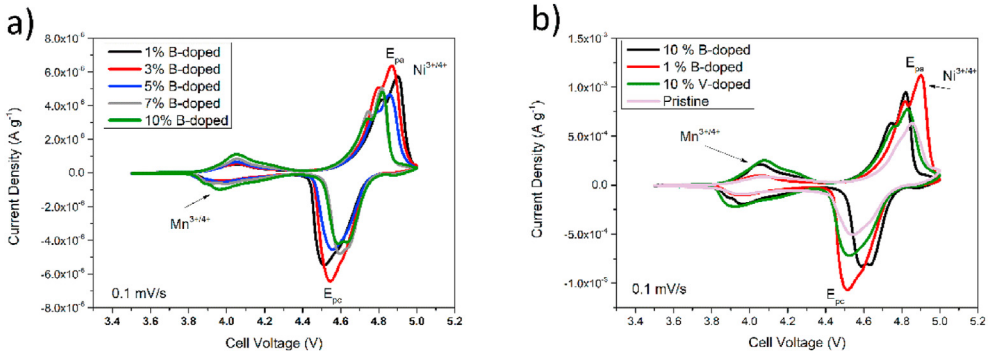

Fig. 5. Cyclic voltammograms of LNMO-based electrodes at 0.1 mV s^{-1} at 25 °C before cycling test of a) pristine, 1% B-doped, 3% B-doped, 5% B-doped, 7% B-doped and 10% B-doped; b) pristine, 1% B-doped, 10% B-doped and 10% V-doped.

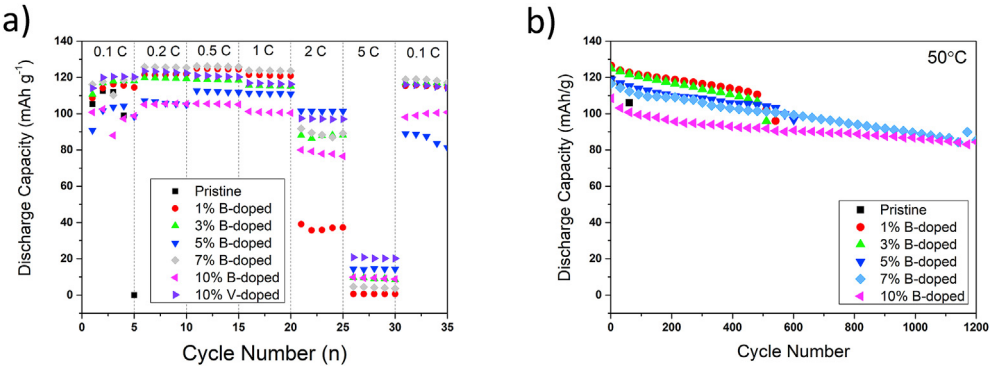

Fig. 6. Rate capability of pristine, 1%, 3%, 5%, 7%, 10% B-doped and 10% V-doped LNMO electrodes at 50 °C, b) cycling performance of pristine, 1 % B-doped, 3 % B-doped, 5 % B-doped, 7 % B-doped, and 10 % B-doped LNMO electrodes at 50 °C and 1C.

(CEI) layers on the new-formed surface [11,28,42]. The 1 % boron doping amount has a huge impact on rate capability compared to the pristine sample at 50 °C. Therefore, doping enhances structural stability, prevents microcracks and rapid cell failure thanks to the stronger bond dissociation energy of the doped element.

The extended cycling performance evinces the advantage of the high doping amount. Fig. 6b shows the comparison of pristine, 1%B-doped, 3%B-doped, 5%B-doped, 7%B-doped, and 10% B-doped LNMO electrodes at 50 °C and 1C up to 1200 cycles. While the pristine cells failed at the beginning of the test, the 7 % B-doped electrode shows a discharge capacity of 117 mAh g^{-1} at the first cycle, which is higher than that of 10 % B-doped (109 mAh g^{-1}). However, 7 % B-doped showed higher capacity fade (23.4 %) than 10 % B-doped (20.5%) after 1200 cycles. The high amount of doping decreases charging the redox processes and duration at ~4.7 V, implicitly reducing the electrolyte decomposition.

Fig. 7a–f shows the voltage profiles at 50 °C and 1C of B-doped LNMO electrodes compared to 10% V-doped LNMO ones. Table 2 shows the discharge capacities in mAh g^{-1}_{LNMO} of pristine, B-doped, and V-doped LNMO electrodes at the 1st, 100th, 200th and 400th cycles. When the boron-doping amount increases, the discharge capacity of the first cycle decreases (127 mAh g^{-1} of 1% B-doped against 109 mAh g^{-1} of 10% B-doped), presumably due to a decrease of the electrochemical process of the Ni redox couples [11]. However, the 10% B-doped LNMO displays the highest capacity retention (Fig. 7e), i.e., 91% after the 100th cycle and 85% after the 400th cycle, calculated with respect to the capacity of the capacity at the first cycle (109 mAh g^{-1}). Similar behavior was demonstrated for 4, 5, and 6 wt % Ti-doped LNMO electrodes that showed lower capacity fade than 1, 2, and 3% Ti-doped after 100 cycles

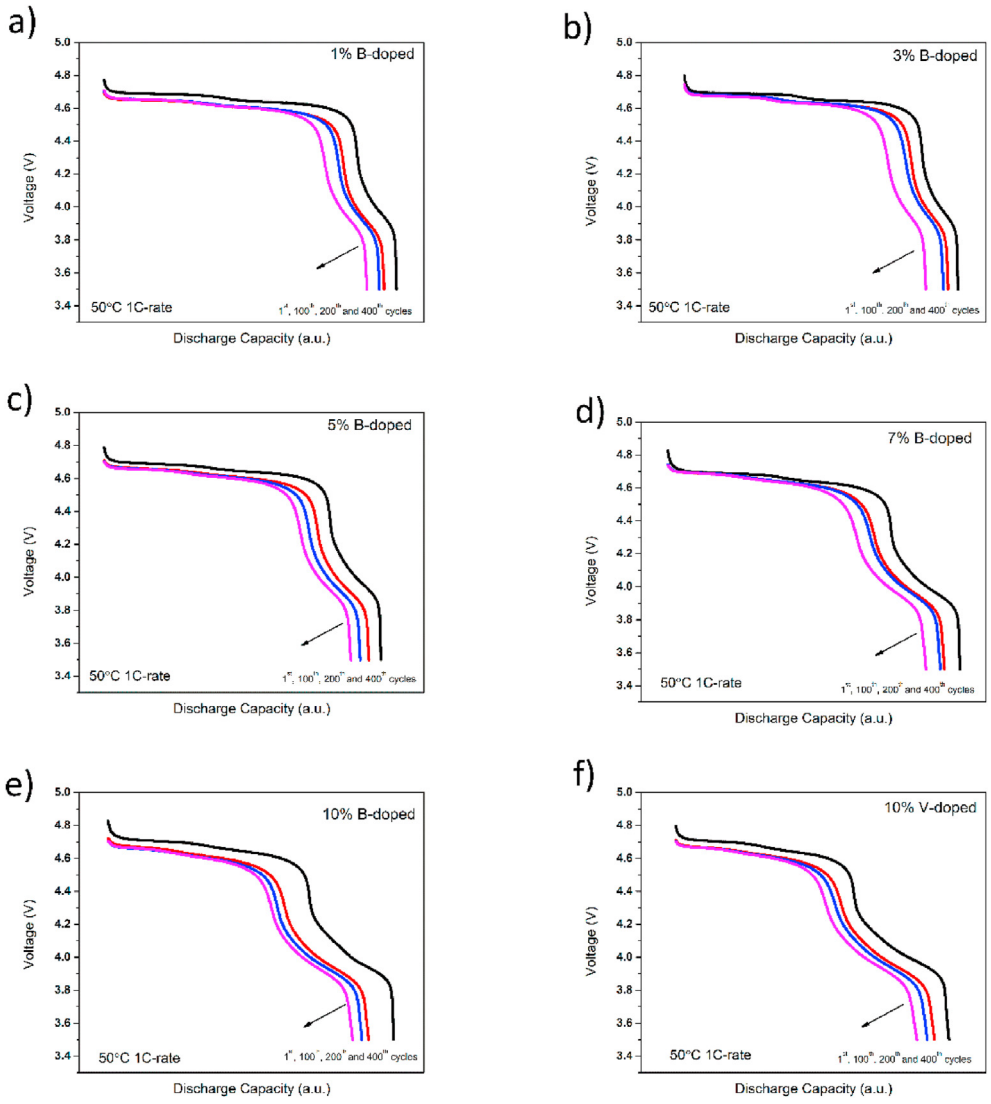

Fig. 7. Voltage profiles of the 1st, 100th, 200th and 400th cycles vs. discharge capacities of a) 1%, b) 3%, c) 5%, d) 7%, e) 10% B-doped and (f) 10% V-doped LNMO electrodes tested at 50 °C and 1C (The discharge capacity values are reported in Table 2.).

Table 2
Discharge capacities of 1%, 3%, 5%, 7%, 10% B-doped and 10% V-doped LNMO electrodes at the 1st, 100th, 200th and 400th cycles, and capacity fade between the 1st and the 100th cycle and the 100th and 400th cycle (50 °C and 1C).

Sample Code	1st cycle discharge capacity	100th cycle discharge capacity	200th cycle discharge capacity	400th cycle discharge capacity	Capacity fade % between 1st and 100th cycles	Capacity fade % between 100th and 400th cycles
Pristine	119.1	Failed	0	0	0	0
1% B-doped	126.5	121.2	119.1	113.8	4.1	6.1
3% B-doped	124.9	120.3	118.2	110.2	3.6	8.3
5% B-doped	118.8	113.7	110	105.9	4.2	6.8
7% B-doped	116.6	110.3	108.6	103.0	5.4	6.6
10% B-doped	108.5	98.9	96.3	92.9	8.8	6.0
10% V-doped	101.8	96.4	93.8	89.9	5.3	6.7

at 60 °C [43]. The high-capacity retention displayed by electrodes with high doping amount might be due to the decreased charge voltage plateau at ~4.7 V and increased at ~4 V. Therefore, decreasing the charging step duration at ~4.7 V causes lower electrolyte decomposition and better cycling performance.

Liang et al. observed that the capacity retention of 10% Mg-doped LNMO at 10 C (6 min for each charging step) is better than at 1 C (60 min for each charging step), i.e., 88.2% vs. 86.3%, respectively, after

1500 cycles [5]. Similarly, Liu et al. demonstrated that pristine LNMO electrodes show 90% capacity retention at 1C, whereas 99% at 5C, 96% at 10C, and 93% at 20C over 2000 cycles at 20 °C that the lowest capacity retention detected at 1C [21]. Therefore, the high C-rate capability of LNMO is inherently better than low C-rates and desired property for high-power applications.

Fig. 8a shows the EIS spectra of all the LNMO-based electrodes. The spectra were recorded in discharge state to compare the resistance values of all the samples. The 5% B-doped sample exhibits the lowest impedance due to the highest amount of Mn^{3+} comparison with other boron-doped samples (Fig. 4b). Similarly, 10% V-doped electrodes, which displayed higher Mn^{3+} content as confirmed by CV results (Fig. 5b), show lower impedance values than pristine since the boron or vanadium doping increases the Mn^{3+}/Mn^{4+} ratio and enhances LNMO's electrical conductivities and rate capability performances [5,15,17,25].

Operando DEMS measurements were performed on 10% B-doped LNMO electrodes to evaluate the gas evolution of H_2 and O_2 increase at ~4.7 V (Fig. 8b). H_2 evolution suggests a close involvement of electrolyte degradation and the transfer of H^+ and electron in the EC solvent decomposition [16]. The evolution of a small amount of O_2 is attributed to structural destabilization via the migration of transition metal (TM) into the empty octahedral sites [17,44]. The Ni^{3+}/Ni^{4+} redox couple plays a crucial role in the gassing of LNMO cells [20]. Indeed, the charging process at high potentials higher than 4.6 V increases electrolyte decomposition and gas evolution that could also leading to battery swelling [11,45].

In order to demonstrate that higher duration time at 4.7 V accelerates the electrolyte decomposition, an additional 5 min-CV charging step at 4.7 V was performed for 10% B-doped LNMO electrodes at 1C and 50 °C (Fig. 8c and Fig. S5). It showed rapid capacity fade and gas evolution at 4.7 V when a 5 min-CV step was added for each charge (Fig. 8d). Aktekin et al. added 2h-CV at 4.95 V for each charging step and observed side reactions and lithium loss [29]. Therefore, the rapid capacity fade can be attributed to electrolyte degradation and gas emissions at ~4.7 V.

Therefore, the DEMS results confirm that high doping amount of boron or vanadium protects the electrode from oxidative electrolyte degradation at potentials higher than 4.7 V due to decreasing $Ni^{4+/3+}$ redox activity. This assumption agrees with the ICP analysis of Fig. 2c that confirms the decrease of Ni wt.% due to an increase of boron wt. %.

4. Conclusions

The doping method is one of the most effective primary strategies to improve the electrochemical performance of $LiNi_{0.5}Mn_{1.5}O_4$ (LNMO)-based electrodes. In the present paper, high temperature (50 °C), relatively high C-rate (1C), and extended cycle life (400 and 1200 cycles) are investigated to reveal the beneficial effect of the doping effect. Two different dissociation bond energy level elements were studied, i.e., B^{3+} and V^{5+}, to prove the effectiveness of the doping elements on cycling performance and rate capability. Although considerable differences were not observed between the two elements on capacity retention performance, the high doping amount (10 wt%) reduces discharge capacity, bringing to two benefits: i) it increases Mn^{3+} amount and increases rate capability, and ii) it reduces voltage plateau at 4.7 V ($Ni^{4+/3+}$ and $Ni^{3+/2+}$), while increasing that at ~ 4 V ($Mn^{4+/3+}$). Therefore, high amount doping implicitly prevents the LNMO electrode from electrolyte decomposition at the electrode/electrolyte interface at high voltage over extended cycles.

Since the real benefits of doping can be observed after 1000 cycles, high temperature (> 50 °C) and extended cycle performance should be applied to reveal the effective benefits of doping.

Conflicts of interest

Potential conflict of interest exists:
No conflict of interest exists.

Funding

This work was supported by the National Natural Science Foundation of China (U1802256,21773118, 21875107), Key Research and Development Program in Jiangsu Province (BE2018122), and Priority Academic Program Development of Jiangsu Higher Education Institutions (PAPD). The authors would also like to thank Dr. Burak Aktekin and Dr. Servet TURAN for helpful technical discussions in designing the experiments that enabled this paper.

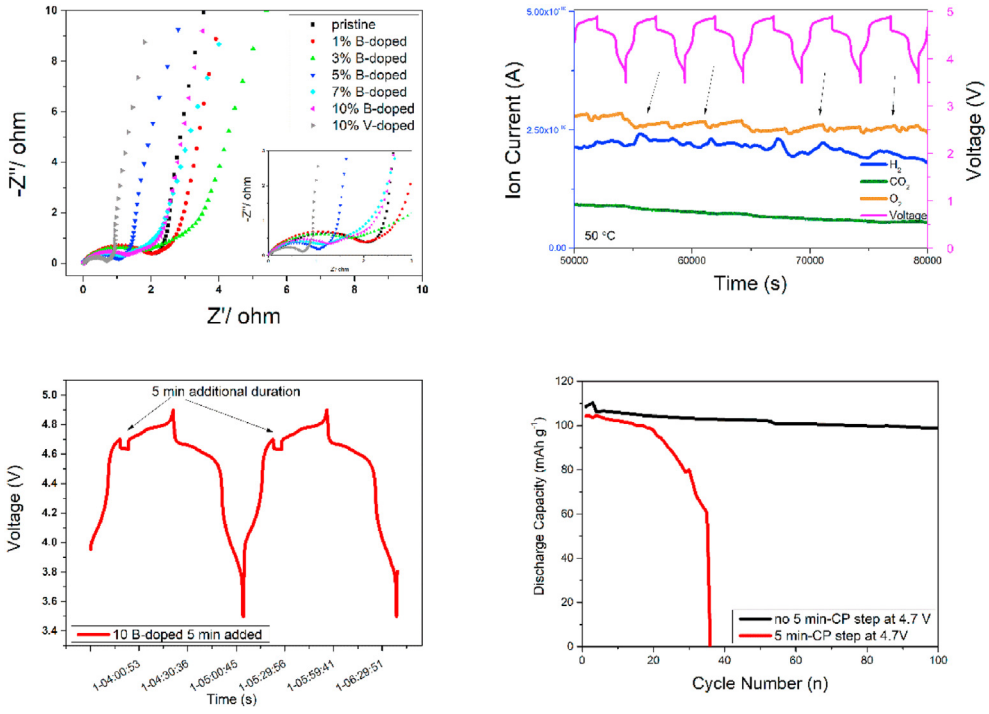

Fig. 8. a) Nyquist plots (recorded in OCV mode and discharge state) of pristine, 1% B-doped, 3% B-doped, 5% B-doped, 7% B-doped, 10% B-doped, and 10% V-doped LNMO electrodes at 25 °C before cycling tests; b) Operando DEMS results of 10% B-doped LNMO electrode tested at 50 °C and 1C, c) Voltage profiles of 10% B-doped LNMO electrodes tested at 50 °C and 1C, charge with additional 5 min-CV step at 4.7 V, d) Comparison of cycling performance of 10% B-doped LNMO electrodes tested at 50 °C and 1C rate with 5 min-CP charging step at 4.7 V (red line) and without 5 min-CV charging step.

Intellectual property

We confirm that we have given due consideration to the protection of intellectual property associated with this work and that there are no impediments to publication, including the timing of publication, with respect to intellectual property. In so doing we confirm that we have followed the regulations of our institutions concerning intellectual property.

Research ethics

We further confirm that any aspect of the work covered in this manuscript that has involved human patients has been conducted with the ethical approval of all relevant bodies and that such approvals are acknowledged within the manuscript.

IRB approval was obtained (required for studies and series of 3 or more cases).

Written consent to publish potentially identifying information, such as details or the case and photographs, was obtained from the patient(s) or their legal guardian(s).

Authorship

All listed authors meet the ICMJE criteria.
We attest that all authors contributed significantly to the creation of this manuscript, each having fulfilled criteria as established by the ICMJE.

One or more listed authors do(es) not meet the ICMJE criteria.

We believe these individuals should be listed as authors because:

We confirm that the order of authors listed in the manuscript has been approved by all named authors.

Contact with the editorial office

This author submitted this manuscript using his/her account in EVISE.

We understand that this Corresponding Author is the sole contact for the Editorial process (including EVISE and direct communications with the office). He/she is responsible for communicating with the other authors about progress, submissions of revisions and final approval of proofs.

We confirm that the email address shown below is accessible by the Corresponding Author, is the address to which Corresponding Author's EVISE account is linked, and has been configured to accept email from the editorial office of American Journal of Ophthalmology Case ReportsSomeone other than the Corresponding Author declared above submitted this manuscript from his/her account in EVISE:

X We understand that this author is the sole contact for the Editorial process (including EVISE and direct communications with the office). He/she is responsible for communicating with the other authors, including the Corresponding Author, about progress, submissions of revisions and final approval of proofs.

Declaration of competing interest

The authors declare that they have no known competing financial interests or personal relationships that could have appeared to influence the work reported in this paper.

Acknowledgments

This work was supported by the National Natural Science Foundation of China (U1802256, 21773118, 21875107), Leading Edge Technology of Jiangsu Province (BK20202008), Key Research and Development Program in Jiangsu Province (BE2018122), and Priority Academic Program Development of Jiangsu Higher Education Institutions (PAPD). The authors would also like to thank Dr. Burak Aktekin and Dr. Servet TURAN for helpful technical discussions in designing the experiments that enabled this paper.

Appendix A. Supplementary data

Supplementary data to this article can be found online at https://doi.org/10.1016/j.jssc.2022.123006.

References

[1] Y.K. Sun, Y.S. Lee, M. Yoshio, K. Amine, Synthesis and electrochemical properties of ZnO-coated $LiNi_{0.5}Mn_{1.5}O_4$ as 5 V cathode material for lithium secondary batteries, Electrochem. Solid State Lett. 5 (2002) 99–102, https://doi.org/10.1149/1.1465375.

[2] I. Tsiropoulos, D. Tarvydas, N. Lebedeva, Li-ion Batteries for Mobility and Stationary Storage Applications, JRC Science for Policy Report, EU Commission., 2018, https://doi.org/10.2760/87175.

[3] X. Liu, X. Zhan, Z.D. Hood, W. Li, D.N. Leonard, A. Manthiram, M. Chi, Essential effect of the electrolyte on the mechanical and chemical degradation of $Li_{0.8}Co_{0.15}Al_{0.05}O_2$ cathodes upon long-term cycling, J. Mater. Chem. A. 9 (2021) 2111–2119, https://doi.org/10.1039/D0TA07814J.

[4] T.F. Yi, Y. Xie, Y.R. Zhu, R.S. Zhu, M.F. Ye, High rate micron-sized niobium-doped $LiNi_{0.5}Mn_{1.5}O_4$ as ultra high power positive-electrode material for lithium-ion batteries, J. Power Sources 211 (2012) 59–65, https://doi.org/10.1016/j.jpowsour.2012.03.095.

[5] G. Liang, Z. Wu, C. Didier, W. Zhang, J. Cuan, B. Li, K.Y. Ko, P.Y. Hung, C.Z. Lu, Y. Chen, G. Leniec, S.M. Kaczmarek, B. Johannessen, L. Thomsen, V.K. Peterson, W.K. Pang, Z. Guo, A long cycle-life high-voltage spinel lithium-ion battery electrode achieved by site-selective doping, Angew. Chem. Int. Ed. 59 (2020) 10594–10602, https://doi.org/10.1002/anie.202001454.

[6] M. Aklalouch, J.M. Amarilla, R.M. Rojas, I. Saadoune, J.M. Rojo, Chromium doping as a new approach to improve the cycling performance at high temperature of 5 V $LiNi_{0.5}Mn_{1.5}O_4$-based positive electrode, J. Power Sources 185 (2008) 501–511, https://doi.org/10.1016/j.jpowsour.2008.06.074.

[7] J. Mao, M. Ma, P. Liu, J. Hu, G. Shao, V. Battaglia, K. Dai, G. Liu, The effect of cobalt doping on the morphology and electrochemical performance of high-voltage spinel $LiNi_{0.5}Mn_{1.5}O_4$ cathode material, Solid State Ionics 292 (2016) 70–74, https://doi.org/10.1016/j.ssi.2016.05.008.

[8] Batteries Europe, Strategic Research Agenda for Batteries, 2020. https://ec.europa.eu/energy/topics/technology-and-innovation/batteries-europe/news-articles-and-publications/sra_en.

[9] M.M. Thackeray, Structural fatigue in spinel electrodes in high voltage (4 V) Li/$Li_xMn_2O_4$ cells, electrochem, Solid-State Lett. 1 (1999) 7, https://doi.org/10.1149/1.1390617.

[10] K. Amine, H. Tukamoto, H. Yasuda, Y. Fuiita, A new three-volt spinel $Li_{1+x}Ni_{0.5}Mn_{1.5}O_4$ for secondary lithium batteries, J. Electrochem. Soc. 143 (1996) 1607–1613.

[11] G. Liang, V.K. Peterson, K.W. See, Z. Guo, W.K. Pang, Developing high-voltage spinel $LiNi_{0.5}Mn_{1.5}O_4$ cathodes for high-energy-density lithium-ion batteries: current achievements and future prospects, J. Mater. Chem. A. 8 (2020) 15373–15398, https://doi.org/10.1039/d0ta02812f.

[12] D.K. Lee, S.C. Han, D. Ahn, S.P. Singh, K.S. Sohn, M. Pyo, Suppression of phase transition in $LiTb_{0.01}Mn_{1.99}O_4$ cathodes with fast Li+ diffusion, ACS Appl. Mater. Interfaces 4 (2012) 6842–6848, https://doi.org/10.1021/am302003r.

[13] J. Ma, P. Hu, G. Cui, L. Chen, Surface and interface issues in spinel: insights into a potential cathode material for high energy density lithium ion batteries, Chem. Mater. 28 (2016) 3578–3606, https://doi.org/10.1021/acs.chemmater.6b00948.

[14] T.F. Yi, J. Mei, Y.R. Zhu, Key strategies for enhancing the cycling stability and rate capacity of $LiNi_{0.5}Mn_{1.5}O_4$ as high-voltage cathode materials for high power lithium-ion batteries, J. Power Sources 316 (2016) 85–105, https://doi.org/10.1016/j.jpowsour.2016.03.070.

[15] A. Wei, J. Mu, R. He, X. Bai, Z. Liu, L. Zhang, Y. Wang, Z. Liu, Enhancing electrochemical performance and structural stability of $LiNi_{0.5}Mn_{1.5}O_4$ cathode material for rechargeable lithium-ion batteries by boron doping, Ceram. Int. (2020), https://doi.org/10.1016/j.ceramint.2020.08.125, 0–1.

[16] K. Leung, Rosy, M. Noked, Anodic decomposition of surface films on high voltage spinel surfaces - density function theory and experimental study, J. Chem. Phys. 151 (2019), https://doi.org/10.1063/1.5131447.

[17] S. Monaco, F. De Giorgio, L. Da Col, M. Riché, C. Arbizzani, M. Mastragostino, Electrochemical performance of $LiNi_{0.5}Mn_{1.5}O_4$ composite electrodes featuring carbons and reduced graphene oxide, J. Power Sources 278 (2015) 733–740, https://doi.org/10.1016/j.jpowsour.2014.12.099.

[18] Y.H. Xu, S.X. Zhao, Y.F. Deng, H. Deng, C.W. Nan, Improved electrochemical performance of 5 V spinel $LiNi_{0.5}Mn_{1.5}O_4$ microspheres by F-doping and Li_4SiO_4 coating, J. Mater. 2 (2016) 265–272, https://doi.org/10.1016/j.jmat.2016.04.005.

[19] J.F. Browning, L. Baggetto, K.L. Jungjohann, Y. Wang, W.E. Tenhaeff, J.K. Keum, D.L. Wood, G.M. Veith, In situ determination of the liquid/solid interface thickness and composition for the li ion cathode $LiNi_{0.5}Mn_{1.5}O_4$, ACS Appl. Mater. Interfaces 6 (2014) 18569–18576, https://doi.org/10.1021/am5032055.

[20] B. Michalak, B.B. Berkes, H. Sommer, T. Bergfeldt, T. Brezesinski, J. Janek, Gas evolution in $LiNi_{0.5}Mn_{1.5}O_4$/graphite cells studied in operando by a combination of differential electrochemical mass spectrometry, neutron imaging, and pressure

measurements, Anal. Chem. 88 (2016) 2877–2883, https://doi.org/10.1021/acs.analchem.5b04696.
[21] H. Liu, R. Kloepsch, J. Wang, M. Winter, J. Li, Truncated octahedral $LiNi_{0.5}Mn_{1.5}O_4$ cathode material for ultralong-life lithium-ion battery: positive (100) surfaces in high-voltage spinel system, J. Power Sources 300 (2015) 430–437, https://doi.org/10.1016/j.jpowsour.2015.09.066.
[22] J. Cao, Z. Ling, X. Fang, Z. Zhang, Delayed liquid cooling strategy with phase change material to achieve high temperature uniformity of Li-ion battery under high-rate discharge, J. Power Sources 450 (2020) 227673, https://doi.org/10.1016/j.jpowsour.2019.227673.
[23] T. Kocak, L. Wu, J. Wang, U. Savaci, S. Turan, X. Zhang, The effect of vanadium doping on the cycling performance of $LiNi_{0.5}Mn_{1.5}O_4$ spinel cathode for high voltage lithium-ion batteries, J. Electroanal. Chem. 881 (2021) 114926, https://doi.org/10.1016/j.jelechem.2020.114926.
[24] J. Wang, P. Nie, G. Xu, J. Jiang, Y. Wu, R. Fu, H. Dou, X. Zhang, High-voltage $LiNi_{0.45}Cr_{0.1}Mn_{1.45}O_4$ cathode with superlong cycle performance for wide temperature lithium-ion batteries, Adv. Funct. Mater. 1704808 (2017) 1704808, https://doi.org/10.1002/adfm.201704808.
[25] H. Liu, X. Zhang, X. He, A. Senyshyn, A. Wilken, D. Zhou, O. Fromm, P. Niehoff, B. Yan, J. Li, M. Muehlbauer, J. Wang, G. Schumacher, E. Paillard, M. Winter, J. Li, Truncated octahedral high-voltage spinel $LiNi_{0.5}Mn_{1.5}O_4$ cathode materials for lithium ion batteries: positive influences of Ni/Mn disordering and oxygen vacancies, J. Electrochem. Soc. 165 (2018) A1886–A1896, https://doi.org/10.1149/2.1241809jes.
[26] T. Ohzuku, K. Ariyoshi, S. Takeda, Y. Sakai, Synthesis and characterization of 5 V insertion material of $Li[Fe_y\ Mn_{2-y}\ ]O_4$ for lithium-ion batteries, Electrochim. Acta 46 (2001) 2327–2336, https://doi.org/10.1016/S0013-4686(00)00725-8.
[27] M. Kunduraci, G.G. Amatucci, Synthesis and characterization of nanostructured 4.7 V $Li_xMn_{1.5}Ni_{0.5}O_4$ spinels for high-power lithium-ion batteries, J. Electrochem. Soc. 153 (2006) A1345, https://doi.org/10.1149/1.2198110.
[28] Z. Chen, R. Zhao, P. Du, H. Hu, T. Wang, L. Zhu, H. Chen, Polyhedral $LiNi_{0.5}Mn_{1.5}O_4$ with excellent electrochemical properties for lithium-ion batteries, J. Mater. Chem. A. 2 (2014) 12835–12848, https://doi.org/10.1039/c4ta02371d.
[29] B. Aktekin, F. Massel, M. Ahmadi, M. Valvo, M. Hahlin, W. Zipprich, F. Marzano, L. Duda, R. Younesi, K. Edström, D. Brandell, How Mn/Ni ordering controls electrochemical performance in high-voltage spinel $LiNi_{0.44}Mn_{1.56}O4$ with fixed oxygen content, ACS Appl. Energy Mater. 3 (2020) 6001–6013, https://doi.org/10.1021/acsaem.0c01075.
[30] G.B. Zhong, Y.Y. Wang, Y.Q. Yu, C.H. Chen, Electrochemical investigations of the $LiNi_{0.45}Mo_{0.10}Mn_{0.0.45}O_4$ (M = Fe, Co, Cr) 5V cathode materials for lithium ion batteries, J. Power Sources 205 (2012) 385–393, https://doi.org/10.1016/j.jpowsour.2011.12.037.
[31] D.W. Kim, H. Shiiba, N. Zettsu, T. Yamada, T. Kimijima, G. Sánchez-Santolino, R. Ishikawa, Y. Ikuhara, K. Teshima, Full picture discovery for mixed-fluorine anion effects on high-voltage spinel lithium nickel manganese oxide cathodes, NPG Asia Mater. 9 (2017) 1–10, https://doi.org/10.1038/am.2017.90.
[32] R. Amin, I. Belharouk, Part I: electronic and ionic transport properties of the ordered and disordered $LiNi_{0.5}Mn_{1.5}O_4$ spinel cathode, J. Power Sources 348 (2017) 311–317, https://doi.org/10.1016/j.jpowsour.2017.02.071.
[33] J. Xiao, X. Chen, P.V. Sushko, M.L. Sushko, L. Kovarik, J. Feng, Z. Deng, J. Zheng, G.L. Graff, Z. Nie, D. Choi, J. Liu, J.G. Zhang, M.S. Whittingham, High-performance $LiNi_{0.5}Mn_{1.5}O_4$ Spinel controlled by Mn3+ concentration and site disorder, Adv. Mater. 24 (2012) 2109–2116, https://doi.org/10.1002/adma.201104767.
[34] M. Malik, K.H. Chan, G. Azimi, Effect of Synthesis Method on the Electrochemical Performance of $LiNi_xMnCo_{1-X-y}O_2$ (NMC) Cathode for Li-Ion Batteries: A Review, Springer International Publishing, 2021, https://doi.org/10.1007/978-3-030-65489-4_5.
[35] F. De Giorgio, N. Laszczynski, J. von Zamory, M. Mastragostino, C. Arbizzani, S. Passerini, Graphite//$LiNi_{0.5}Mn_{1.5}O_4$ cells based on environmentally friendly made-in-water electrodes, ChemSusChem 10 (2017) 379–386, https://doi.org/10.1002/cssc.201601249.
[36] L. Li, J. Sui, J. Chen, Y. Lu, LiNi 0.5 Mn 1.5 O 4 microrod with ultrahigh Mn 3+ content: a high performance cathode material for lithium ion battery, Electrochim. Acta 305 (2019) 433–442, https://doi.org/10.1016/j.electacta.2019.03.086.
[37] Y. Ben Smida, R. Marzouki, S. Kaya, S. Erkan, M. Faouzi Zid, A. Hichem Hamzaoui, Synthesis methods in solid-state chemistry, Synth. Meth. Cryst. (2020), https://doi.org/10.5772/intechopen.93337.
[38] J. Liu, A. Manthiram, Understanding the improved electrochemical performances of Fe-substituted 5 V spinel cathode $LiMn_{1.5}Ni_{0.5}O_4$, J. Phys. Chem. C 113 (2009) 15073–15079, https://doi.org/10.1021/jp904276t.
[39] L. Wang, D. Chen, J. Wang, G. Liu, W. Wu, G. Liang, Improved structural and electrochemical performances of $LiNi_{0.5}Mn_{1.5}O_4$ cathode materials by Cr^{3+} and/or Ti^{4+} doping, RSC Adv. 5 (2015) 99856–99865, https://doi.org/10.1039/C5RA20003B.
[40] H. Wang, H. Xia, M.O. Lai, L. Lu, Enhancements of rate capability and cyclic performance of spinel $LiNi_{0.5}Mn_{1.5}O_4$ by trace Ru-doping, Electrochem. Commun. 11 (2009) 1539–1542, https://doi.org/10.1016/j.elecom.2009.05.054.
[41] J. Deng, Y. Xu, L. Xiong, L. Li, X. Sun, Y. Zhang, Improving the fast discharge performance of high-voltage $LiNi_{0.5}Mn_{1.5}O_4$ spinel by Cu^{2+}, Al^{3+}, Ti^{4+} tri-doping, J. Alloys Compd. 677 (2016) 18–26, https://doi.org/10.1016/j.jallcom.2016.03.256.
[42] J. Akimoto, Y. Hamada, N. Ishida, Y. Idemoto, Y. Matsushita, K. Kataoka, Structural change and morphological surface degradation upon electrochemical Li extraction from a single crystal of spinel-type $LiNi_{0.5}Mn_{1.5}O_4$, Cryst. Growth Des. 20 (2020) 4533–4539, https://doi.org/10.1021/acs.cgd.0c00327.
[43] M. Lin, S.H. Wang, Z.L. Gong, X.K. Huang, Y. Yang, A strategy to improve cyclic performance of $LiNi_{0.5}Mn_{1.5}O_4$ in a wide voltage region by Ti-doping, J. Electrochem. Soc. 160 (2013) A3036–A3040, https://doi.org/10.1149/2.004305jes.
[44] M. Lin, L. Ben, Y. Sun, H. Wang, Z. Yang, L. Gu, X. Yu, X. Yang, H. Zhao, R. Yu, M. Armand, X. Huang, Insight into the atomic structure of high-voltage spinel $LiNi_{0.5}Mn_{1.5}O_4$ cathode material in the first cycle, Chem. Mater. 27 (2015) 292–303.
[45] D. Aurbach, B. Markovsky, Y. Talyossef, G. Salitra, H.J. Kim, S. Choi, Studies of cycling behavior, ageing, and interfacial reactions of $LiNi_{0.5}Mn_{1.5}O_4$ and carbon electrodes for lithium-ion 5-V cells, J. Power Sources 162 (2006) 780–789, https://doi.org/10.1016/j.jpowsour.2005.07.009.